Chapter 2.
Experimental: processes, principles and characterization

2.1 Introduction

Nanotechnology enables the manipulation and control of individual and clusters of atoms and creates novel materials useful for a vast range of current applications. A crucial factor influencing the use and functionality of nanoscale materials across various fields is the method by which nanostructures and nanomaterials are synthesized and grown. The specific growth and fabrication processes employed are closely connected to the structure and morphology of nanomaterials. In recent years, numerous innovative devices and patentable technologies have emerged, particularly those based on two-dimensional (2D) layered nanomaterials [1,2].

To synthesize nanostructured materials, bottom-up and top-down are the two main methods used. The bottom-up approach is a constructive technique where one smaller component of atomic or molecular dimensions becomes a nucleating agent to favour self-assembly and aggregation. Through this process, nanomaterials with distinct sizes, shapes, and chemical compositions are formed. This method includes some sophisticated procedures and encompasses chemical vapour deposition (CVD), laser CVD (LCVD), co-precipitation, hydrothermal, and sol-gel methods. In contrast, top-down approaches are scalable, user-friendly and much more cost-effective. Through this method, bulk material can be transformed into small nano-sized particles. Some of the common top-down approaches to synthesise nanomaterials include mechanical exfoliation, sonication-assisted liquid phase exfoliation, thermal evaporation, ball milling, sputtering, laser ablation, etc. [3].

Transition metal dichalcogenides (TMDCs) are well-known pseudo-2D materials in their bulk form, consisting of stacked layers held together by weak van der Waals interactions, while the atoms within each layer are covalently bonded. A well-known technique for exfoliating these layers is the Scotch-tape method, which contributed to the discovery of graphene in 2004 [4]. However, this method is impractical for producing a large amount of material required for numerous applications. As a result, liquid-phase based exfoliation has become the most commonly used method for generating few-layer TMDCs and has gained widespread implementation in recent decades. This method is especially important for applications of TMDCs where reactions occur at the surface or between layers, rather than throughout the bulk structure [5].

Moreover, TMDCs are gaining importance in the field of cutting-edge composite materials, mainly in polymer nanocomposites. The incorporation of TMDCs into polymer

matrices can improve the thermal stability and mechanical strength of the composite system. This effective integration creates a promising pathway for developing robust, lightweight materials that are well-suited for their use in flexible electronics, aerospace engineering, automotive industry, and a range of other advanced technological assets [6].

Members of the TMDCs family, particularly WS_2 and WSe_2, have garnered considerable interest recently. Compared to their molybdenum (Mo)-based counterparts, tungsten (W) is more abundant in the Earth's crust, making it more cost-effective. The relatively larger atomic size of W can significantly influence the properties of TMDCs. The exfoliation of TMDCs enables the separation of atomically thin layers from their bulk counterparts and warrants exploration of their extraordinary properties. In particular, the layered structure of WS_2 can be potentially exfoliated into distinct layers [7]. Numerous properties, namely, mechanical, optical, and electronic properties, are likely to be influenced by taking advantage of their reduced dimension and surface functionality.

The materials and synthesis process adopted have been elaborated. It also summarizes the basic principles of various instruments and experimental techniques employed for the analysis of prepared samples. Moreover, the preparation of polymeric nanocomposite systems has been discussed by considering WS_2 as a nanofiller in the host matrix. Additionally, the development of fractal-like features in the WS_2/NaCMC nanocomposite films is also highlighted at the end of this chapter.

2.2 Liquid-phase exfoliation (LPE) of tungsten disulfide (WS_2) and tungsten diselenide (WSe_2) systems

Analytical grade tungsten disulfide (WS_2) with 99% purity, grain size of < 2 μm and tungsten diselenide (WSe_2, 99.8 %, metal basis) of grain size <10-20 μm were purchased from Sigma Aldrich®, Propan-2-ol (isopropanol, IPA, extra-pure) from FINAR® chemicals, and N-methyl-2-pyrrolidone procured from EMPLURA® through a local vendor (Zenith, India) were used without further purification.

In this thesis, both IPA/water (co-solvent strategy) and N-methyl-2-pyrrolidone (NMP) were employed to exfoliate bulk WS_2 and WSe_2 materials individually, which are further explored in the subsequent chapters. For the IPA/water co-solvent method, 0.32 g of bulk WS_2 was measured and added to a beaker containing a 30% IPA solution. Similarly, 0.15 g of bulk WS_2 was dispersed in 50 mL of NMP solution. In both cases, the

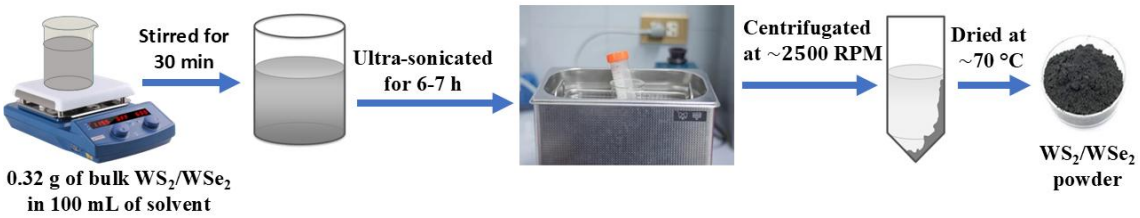

Figure 2.1: The schematic represents the various steps of the liquid phase exfoliation technique to exfoliate bulk WS_2 or WSe_2 material into nanosystems.

solutions of the mixtures were vigorously stirred for over 30 minutes using a magnetic stirrer to achieve homogeneity. Following this, the solutions were subjected to ultrasonic agitation for ~6-7 hours using a water bath sonicator (power 100 W, frequency 40 kHz, RoHS®). To prevent overheating, the water in the bath sonicator was replaced roughly every 30 minutes. After sonication, the samples were washed several times with ethanol and deionized (DI) water and centrifuged at ~2500 RPM for ~15 min. The resulting precipitates of WS_2 nanosheets were then dried in a hot-air oven (REMI®) maintained at ~60-70 °C. Likewise, bulk WSe_2 was exfoliated into nanosheets following similar steps. The schematic representation of various steps of LPE followed to obtain nanosheets of WS_2 or WSe_2 systems from the bulk material, is shown in Fig. 2.1. The exfoliated WS_2 and WSe_2 nanosheets obtained through this process were used for irradiation experiments discussed in the subsequent chapters.

2.3 Characterization techniques

2.3.1 Powder X-ray diffraction

The discovery of X-rays led to the most sought and potent tool, which has revolutionized the entire world of materials science and engineering. Wilhelm Conrad Roentgen discovered X-rays in 1895. Now it is considered to be one of the finest techniques to examine details of any material, spanning its application from material science to chemical and biomedical fields. A precise study of the structure of crystalline phases of the materials can be investigated with the X-ray diffraction (XRD) technique based on the capability of crystals to diffract X-rays characteristically. Recorded diffraction patterns hold contributions from several micro- and macrostructural features of the sample under study. The XRD methods can be utilised to investigate the lattice parameters, chemical composition, peak positions, micro strain, space group, or qualitative phase analysis of the materials. Additionally, quantitative phase analyses can be done based on the peak

intensity to attain details of the crystal structure along with the texture of the sample. Furthermore, XRD patterns can reveal peak broadening due to instrumental broadening, microstrain, and grain size. While the causes of peak broadening can be examined through peak shape analysis, providing insights into the contributions from microstrain and crystallite size [8].

When monochromatic X-rays are diffracted at specific angles by a set of lattice planes within a sample, they undergo constructive interference, resulting in distinct XRD peaks. In an X-ray tube, the electrons originate from either a tungsten or molybdenum filament, which emits them via thermionic emission when a voltage of around 40 kV is applied. These electrons are then accelerated toward a metal anode due to the high voltage applied across the electrodes. When a metal anode, such as copper, is bombarded with electrons, electrons in its innermost shell (first orbit) are ejected. This prompts electrons from the second orbit to jump to the empty space of the innermost orbit (K shell), releasing energy in the form of X-rays. These X-rays are subsequently filtered to process monochromatic radiation, collimated, and directed toward the sample. As the X-rays strike the sample, they interact with the electron cloud surrounding the atoms, scattering in various directions. While most of these scattered waves interfere destructively and cancel each other out, in specific directions defined by Bragg's law, they interfere constructively, producing detectable diffraction peaks [9],

$$n\lambda = 2d \sin \theta_{hkl} \tag{2.1}$$

where '*n'* is the integer, the wavelength of X-rays is denoted by 'λ', the spacing between two crystal planes is denoted by '*d*', and the incident angle of X-rays is represented by 'θ_{hkl}'. The detector captures the diffracted patterns and processes them into a count rate, which is then sent to a device such as a monitor for display.

Moreover, by applying Bragg's law to X-ray reflections, the interplanar spacing d_{hkl} between the (hkl) planes can be determined, which is essential for calculating the lattice parameters. The relationship between d_{hkl} and the Miller indices depends on the crystal system, and for the cubic system, it takes the form [10],

$$\frac{1}{d_{hkl}^2} = \frac{h^2+k^2+l^2}{a^2} \tag{2.2}$$

In the tetragonal system, d_{hkl} relation can be expressed as [10],

$$\frac{1}{d_{hkl}^2} = \frac{h^2+k^2}{a^2} + \frac{l^2}{c^2} \quad (2.3)$$

And, for an ideal hexagonal crystal, the expression for d_{hkl} is given by [11],

$$\frac{1}{d_{hkl}^2} = \frac{4}{3}\left(\frac{h^2+hk+k^2}{a^2}\right) + \frac{l^2}{c^2} \quad (2.4)$$

where a and c represent the lattice parameters, which can be determined from the measured values of d_{hkl}.

XRD patterns were acquired using a powder X-ray diffractometer, Bruker AXS D8 Focus, equipped with CuK_α radiation of wavelength (λ) = 1.5406 Å, operated with a current of 30 mA and accelerating voltage of 30 kV. The measurements were conducted at a scan rate of 1°/min with Bragg's diffraction angle, 2θ, in the range of ~10°-80°. The diffraction peaks are analyzed with the help of JCPDS/ICDD files for appropriate indexing of the crystallographic planes.

2.3.2 UV-visible spectroscopy

Ultraviolet (UV)-visible spectroscopy is an absorption spectroscopy where molecules absorb light in the UV-visible range, causing electrons to transition from lower to higher energy levels. This method is commonly used to characterize composite material systems, semiconductor nanocrystals, and organic semiconductors for a wide range of applications [12].

When light passes through matter, it can be absorbed, which results in an attenuation of the intensity. The probability of absorption is dependent on the wavelength, material, and distance which the photons travel through the material. In the simplest method, absorption can be defined by the Beer-Lambert law [13],

$$I(s) = I_0 e^{-\alpha.s} \quad (2.5)$$

therein, I and I_0 are the intensities of the attenuated and incident light beams, α is a coefficient which depends on the material and wavelength, and s is the thickness of the sample (i.e., the distance that the photons move in the material). The product $\alpha.s$ is generally called optical density or absorbance.

The absorbance spectra were recorded using a UV-visible spectrophotometer (Lambda 365, PerkinElmer®).

2.3.3 Photoluminescence spectroscopy

Photoluminescence (PL) spectroscopy is a technique used for studying the radiative recombination processes in photoexcited semiconductors. This form of optical characterization plays a fundamental role in evaluating semiconducting materials, making it essential for a wide range of optoelectronic applications.

When a crystalline solid is irradiated with monochromatic light whose energy exceeds the band gap, it absorbs this energy and generates electron–hole pairs. These excited electrons and holes typically relax to the edges of the conduction and valence bands, respectively, releasing their excess energy into the lattice as phonons. If the electrons and holes then recombine radiatively at the band edges, photons are emitted with an energy nearly equal to the band gap of the material. This phenomenon is known as near band-edge (NBE) photoluminescence. Radiative recombination can also occur when charge carriers are trapped in defect states. In such cases, photons with energies lower than the band gap are emitted, termed as defect-mediated emission (DE). Detecting these photons through photoluminescence (PL) spectroscopy provides insights into the nature of crystal defects present in the material [14,15]. Emissions suppressed at room temperature may evolve at low temperatures due to adequate reduction in phonon scattering.

Time-resolved photoluminescence spectroscopy (TRPL) is a widely used technique for studying the dynamics of electronic processes. Many of these processes, such as electronic state transitions and charge transfer, occur on ultrafast timescales, typically in the nanosecond, picosecond, or femtosecond range. In TRPL, the sample is excited with a short laser pulse, and the subsequent decay of the photoluminescence (PL) signal is recorded, varying with time. By analyzing these time-dependent PL decay curves, one can extract quantitative information such as decay constants. This analysis often assumes exponential decay behaviour, which simplifies evaluation, especially when only a single decay process is present, allowing for fitting with an equation (2.6) [16],

$$\ln\big(\mathrm{PL}(t)\big) = \ln\big(\mathrm{PL}(t_0)\big) - \frac{1}{\tau}.t \qquad (2.6)$$

Therein, PL(t_0) and PL(t) are the PL signal intensities at the time t_0 and t, respectively, and τ is the time constant of the decay process as a fitting parameter. However, a mono-exponential decay model does not always adequately fit the experimental data. In such cases, more complex models involving multiple fitting parameters are necessary.

Photoluminescence (PL) spectra were acquired using a photoluminescence spectrophotometer (HORIBA QuantaMaster 8450-22). Additionally, a pico-second lifetime spectrophotometer (model: Lifespec II, Edinburg Instruments) was used to obtain decay profiles of time-resolved photoluminescence (TRPL) spectra.

2.3.4 Raman spectroscopy

Raman spectroscopy is an efficient non-destructive technique based on the interaction of light and chemical bonds present within the material. It has proven to be used as a fingerprint technique for characterization of 2D materials. It is used to identify the vibrational modes of the material. This technique employed used to obtain the bonding, conformation, chemical structure, and intermolecular interactions between the molecules. The Raman active modes arise when there is a change in polarizability induced by lattice atoms in the molecule under consideration. The underlying principle involves the inelastic scattering of monochromatic light by matter. It is based on the Raman scattering effect discovered by Indian scientist Sir Chandrasekhara Venkata Raman in the year 1931. In inelastic scattering, photons from monochromatic light undergo changes in frequency when they interact with a sample. This technique involves collecting the scattered light from the material and analyzing it using a spectrometer. If the frequency of the scattered light remains the same as that of the incident light, the scattering is elastic and known as

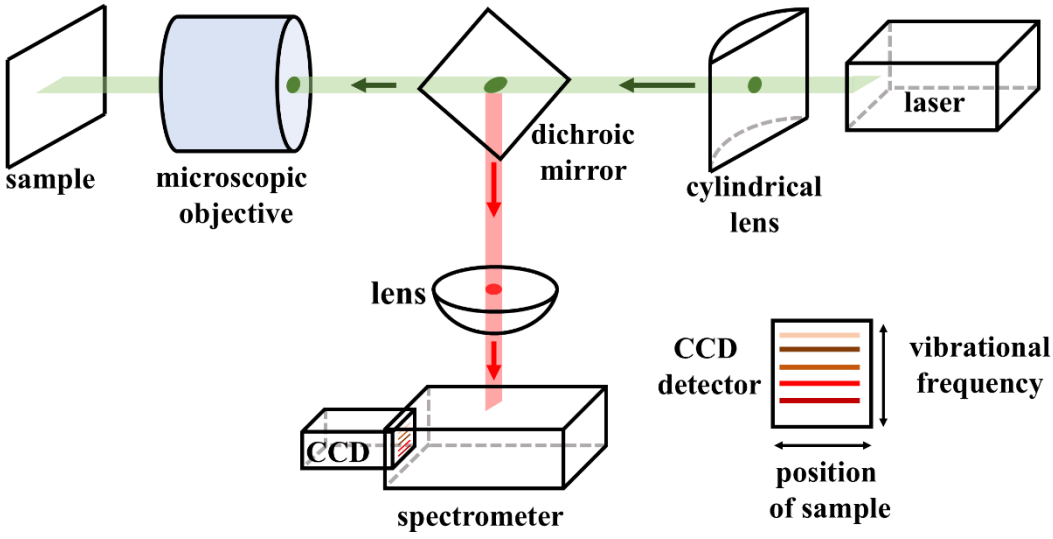

Figure 2.2: The schematic representation of the components in a Raman spectrometer.

Rayleigh scattering. In contrast, Raman scattering occurs when a molecule absorbs a photon, causing its electrons to be excited to a virtual energy state. As the electrons return to the ground state, they emit photons in a process known as stimulated emission. If the energy of the scattered photon is lower than that of the incident photon, the resulting lines are called Stokes lines. If the energy is higher, they are referred to as anti-Stokes lines. The resulting shifts in wavenumber, known as Raman shifts, contain valuable analytical information that reflects the differences between specific quantum energy levels, which are crucial for material identification. These shifts are determined by the molecular structure of the material and are independent of the wavelength of the incident light [17]. A schematic of the Raman spectrometer is shown in Fig. 2.2.

Raman spectra were captured on a Renishaw spectrometer (RENISHAW BASIS SERIES) attached with a 514 nm laser and micro-Raman spectroscopy (EZRaman-N®) equipped with a continuous wave diode laser with a wavelength of 785 nm, and in the range of 100-2000 cm^{-1}.

2.3.5 X-ray photoelectron spectroscopy (XPS)

X-ray photoelectron spectroscopy (XPS) is regarded as one of the best analytical technique for surface characterization and compositional analysis of a material. It is based on the photoelectric effect, first discovered by Heinrich Hertz in 1887, and the concept was formally described by Albert Einstein in 1905. However, Kai Siegbahn developed the X-ray photoelectron spectroscopy into the technique at the University of Uppsala in Sweden in the 1950s-1960s. When X-rays are bombarded onto the surface of a material, electrons are emitted. The kinetic energy of these emitted electrons is measured. The ability to reveal information about the chemical state and surface sensitivity of the elements present in the sample is the two chief characteristics of this technique that make it powerful as an analytical method. This technique provides an elemental analysis of the top 10-200 Å of any solid surface, which is vacuum compatible, except for hydrogen and helium.

In XPS, the material is exposed to soft X-rays of energies lower than ~6 keV, and the kinetic energy of the emitted electrons is measured. When the X-ray energy is entirely transferred to a core-level electron, the photoelectron is emitted. This is stated mathematically as shown in Eq. (2.7). It simply states that the energy of the X-ray ($h\nu$) is equal to the binding energy (BE) of the electron, plus the kinetic energy (KE) of the

electron that is emitted, plus the spectrometer work function ($\Phi_{spec.}$), a constant value calculated through calibration [18],

$$h\nu = \mathrm{BE} + \mathrm{KE} + \Phi_{spec.} \tag{2.7}$$

To determine the binding energy of an electron, Eq. (2.7) can be rearranged to obtain Eq. (2.8), where the terms on the right are either known ($h\nu$ and $\Phi_{spec.}$) or K.E. measured in the XPS experiment,

$$\mathrm{BE} = h\nu - \mathrm{KE} - \Phi s_{pec.} \tag{2.8}$$

An XPS instrument consists of a sample stage, an X-ray source, extraction lenses, an analyzer, and a detector, all enclosed within an ultra-high vacuum chamber. These systems typically operate at very low base pressures, around 10^{-9}–10^{-10} mbar. The X-ray sources are commonly equipped with Mg and/or Al, often configured as a dual-anode system that allows for the selection of either Mg or Al anodes. Positioned between the sample and the analyzer, a set of electron optics, known as extraction lenses, controls the acceptance angle that captures electrons emitted from the sample surface [19].

X-ray Photoelectron Spectroscopy (XPS) surface analysis was carried out using the PHI 5000 VersaProbe III mode from IIT, Roorkee and the AXIS Supra at IIT, Delhi.

2.3.6 Atomic-force microscopy (AFM)

Atomic force microscopy (AFM) is a powerful technique employed to characterize the surface properties, microstructures, etc. of a material on the length scale of submicron to nanometer level. This microscopy is based on the fundamental principle of scanning the surface with a sharp conducting tip (probe) for imaging the surface of a material. The AFM provides a 3D profile on a nanoscale, by measuring forces between the surface at a probe-sample separation of 0.2-10 nm and a sharp probe of radius less than 10 nm. The probe is supported on a flexible cantilever, and the AFM tip gently touches the surface and records the small force between the probe and the surface. The interaction between the probe and the sample is dependent on the forces involved in the tip-sample interaction. If repulsive forces are dominant, the probe remains in direct contact with the surface, identified as contact mode. If the probe is positioned away from the surface, attractive forces become stronger, leading to a non-contact mode operation. AFM primarily operates in three imaging modes: contact mode, with a tip-sample distance of less than 0.5 nm, intermittent

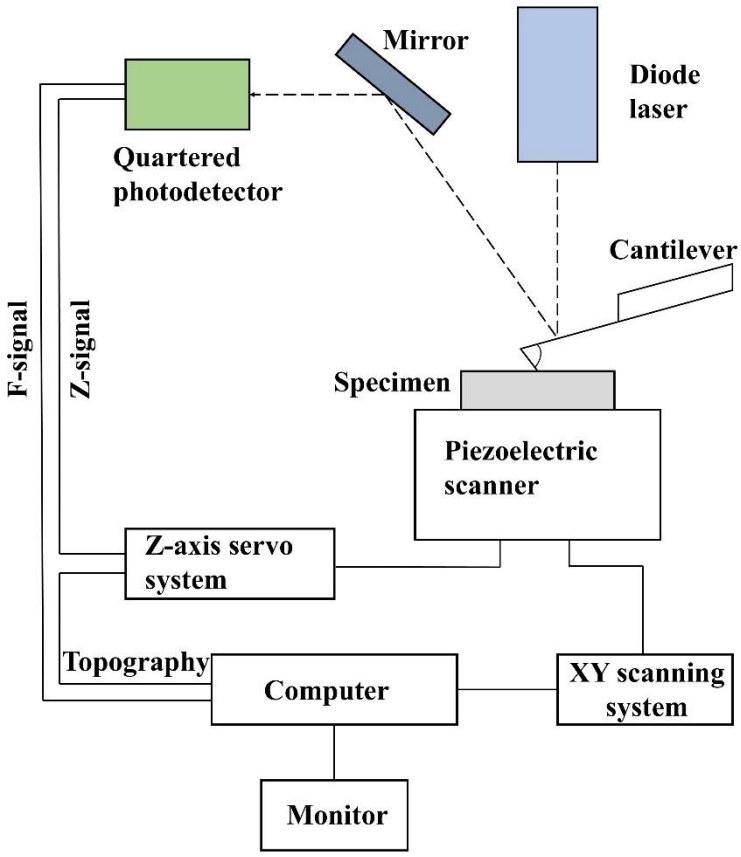

Figure 2.3: Schematic representation of the AFM.

contact mode, where the separation lies between 0.5 nm and 2 nm, and non-contact mode, with distances ranging from 0.1 nm to 10 nm.

The tip and the cantilever can be fabricated from silicon or silicon nitride (Si_3N_4) using photolithographic techniques as a key component. A single silicon wafer can yield over 1,000 individual probes. In terms of physical dimensions, cantilevers generally measure between 100-200 µm in length, 10-40 µm in width, and 0.3-2 µm in thickness [20]. The schematic representation of the AFM is displayed in Fig. 2.3. Researchers also prefer to use carbon nanotubes (CNT) over conventional tips owing versatility and strength.

The surface topography of the systems under consideration was captured by an atomic force microscope (AFM, NTEGRA Prima®, ND-MDT Technology). The scanning was done over a scan area of 10×10 μm^2 and 2.5×2.5 μm^2 in a semi-contact mode with a Si tip of dia. 10 nm and adjusted to a height of 14-16 µm from the specimen surface.

2.3.7 Field-emission scanning electron microscopy (FE-SEM)

Scanning electron microscopy (SEM) is a highly versatile and widely used technique for analyzing surface morphology, microstructural texture, voids, and defects. In SEM, a focused beam of electrons scans the surface of a specimen, generating images using either backscattered or secondary electrons. These electrons are emitted from a tungsten filament cathode via thermionic emission, typically operating at energies between 0.2 and 40 kV. Electromagnetic fields are used to precisely direct the high-energy electron beam onto the specimen, with the SEM optical column ensuring consistent energy and trajectory for the incoming electrons. When the electron beam interacts with the specimen, both elastic and inelastic collisions occur. Electrons that elastically scatter off the atomic nuclei at large angles (ranging from 0° to 180°) are known as backscattered electrons. The intensity of these backscattered electrons depends on the atomic number of the material.

In contrast, when the high-energy beam strikes the surface, it can dislodge loosely bound electrons, producing what are known as secondary electrons. Since secondary electrons are emitted from a depth of about 5 to 50 nm, highly detailed images of the surface morphology can be obtained. To detect both secondary electron and backscattered electron signals, a positive voltage is applied to a collector positioned in front of the detector. Applying a negative voltage to the collector selectively repels secondary electrons, allowing only backscattered electrons to be collected. The captured electron signals are then amplified using a photomultiplier and displayed on a cathode-ray tube, creating detailed images of the specimen [21,22].

In addition to backscattered and secondary electrons, X-rays and Auger electrons are also produced due to scattering interactions. By analyzing the wavelengths of these X-rays, the elemental composition of the material can be identified, a technique known as Energy Dispersive X-ray Spectroscopy (EDX). A more advanced form of SEM is the Field Emission Scanning Electron Microscope (FE-SEM), which uses a field emission gun to generate electrons. This results in a much narrower and more focused electron beam, producing images with higher resolution, greater clarity, and minimal electrostatic distortion.

SEM images and EDX measurements were attained from a scanning electron microscope of model JEOL, JSM 6390 LV with a 20 kV accelerating voltage at Tezpur University.

FE-SEM images were captured from the JEOL JSM 7200F installed at SAIC, Tezpur University and the SIGMA VP FESEM, ZEISS at IASST, Guwahati.

2.3.8 High-resolution transmission electron microscopy (HR-TEM)

The most powerful imaging technique to reveal internal details of material is high-resolution transmission electron microscopy (HR-TEM). It is a technique employed to analyze nanostructured materials, capable of probing atomic arrangements and internal microstructures with a resolution down to 0.1 nm. The process is conducted under high vacuum conditions, where a stream of electrons are continuously emitted from a tungsten (W) or $LaBaO_6$ filament serving as the cathode. When a high voltage, typically between 40 and 400 kV, is applied to the anode, it accelerates the electrons, which are then focused using electrostatic and electromagnetic lenses to pass through the sample. The electrons transmitted through the specimen are captured by imaging systems such as fluorescent screens, photographic film, or digital detectors like CCD cameras. Before being recorded, the transmitted beams are magnified and focused by the objective lenses, and the final image is displayed on a computer monitor. The resolution of the image is determined by the objective lenses, while magnification is adjusted by the projector lenses. Additionally, the wavelength of the electron beam and energy influence both resolution and magnification substantially [23].

Beyond imaging, HR-TEM can also provide a diffraction pattern through a technique called Selected Area Electron Diffraction (SAED). In this method, the electron beam is focused on a specific region of the sample to produce a diffraction pattern, which reveals information about the crystallinity of the material.

The TEM imaging has been performed on a transmission electron microscope installed at the sophisticated analytical instrumentation centre (SAIC) at Tezpur University and IASST, Guwahati. The model of the former utilized is TECNAI G2 20 S-TWIN (200 kV) (FEI COMPANY, USA) with a resolution of 2.4 Å, working at an accelerating voltage of 200 kV. And the later one is JEM-2100 PLUS (HR), JEOL, and the accelerating voltage was 200 kV. The sample preparation for imaging was carried out by dispersing a pinch of sample in 3 mL of ethanol, followed by adequate sonication (40 kHz) to ensure separation of specimen constituents. Then the solution was drop-cast onto a carbon-coated copper grid (400 mesh) for imaging purposes.

2.3.9 Nitrogen (N_2) adsorption-desorption technique

Nitrogen (N_2) adsorption-desorption isotherms are obtained at 77 K and are commonly used to analyze the porous structure of materials. Depending upon size range, porous materials can be categorised into three types: macroporous, mesoporous and microporous [24]. The sample chamber is evacuated at a temperature between 120-200 °C to remove any adsorbed contaminants, then cooled to the temperature of liquid nitrogen (LN_2), before the measurement is carried out. During the adsorption phase, nitrogen gas is introduced gradually, increasing the pressure up to the saturation pressure (P_0). In the desorption phase, the pressure is reduced step by step back to its initial value. At each equilibrium point, the volume of nitrogen adsorbed and desorbed is recorded. These values are then plotted against the relative pressure (P/P_0) to generate an adsorption-desorption isotherm. This curve provides key insights into the porous nature of a material. Additionally, pore size distribution is typically derived from these gas sorption measurements, with classification based on IUPAC standards that relate pore types to specific isotherm shapes.

One of the most widely used methods to estimate the specific surface area of a material from this technique is the Brunauer–Emmett–Teller (BET) model. In addition to surface area, porosity can also be analyzed using various theoretical models such as, Barrett–Joyner–Halenda (BJH), Dollimore–Heal (D–H), Horvath–Kawazoe (HK), and Density Functional Theory (DFT), all of which help interpret physisorption data to determine pore size and pore volume [25].

N_2 adsorption-desorption isotherms were acquired on a Quanta chrome (NOVA 1000e®) analyzer at a liquid N_2 temperature of 77 K. The BJH model was considered to examine the pore volume and pore size distribution based on the desorption data for the samples under study.

2.3.10 Universal Testing Machine (UTM)

A Universal Testing Machine (UTM) is an apparatus used to evaluate the mechanical properties of a solid sample by applying tensile, compressive, or shear stresses on a specimen to be tested. The most common types of UTMs are compressive strength and tensile tests. Further, UTM can also be used to perform standard tests such as bending, pull-out, adhesion, as well as hysteresis tests. Through various testing methods, the UTM helps assess how raw materials or components respond under different stress conditions,

providing insights into their physical and mechanical characteristics. UTM are often used to test composite materials made by combining two substances with distinct physical and chemical properties. The resulting composite materials are modified to exhibit enhanced properties such as increased strength, reduced weight, and improved stiffness, making them suitable for specific applications. UTMs are used to measure critical parameters of composites, including peak load, peak displacement, tensile strength, yield point, and elongation.

A typical universal testing machine consists of two main parts: (a) the loading unit, which handles the specimen setup and applies the load, and (b) the control unit, which reports the loading process and records the data to be tested. UTMs can be used to determine a wide range of mechanical properties, such as shear strength, compressive strength, flexural strength, bending behaviour, etc., across various materials [26,27].

The tensile properties of the free-standing films were analyzed using a universal testing machine (Tinius Olsen, H5KL) and following the ASTM D638↗ method (standard test method for examining tensile properties of plastics). The testing was done at a gauge length of 10 mm, and the applied speed was 5 mm/min with a load cell capacity of 2.5 kN. The thickness of the films was estimated using an electronic micrometer (Schut, Germany). The thickness of the films varied from 0.025-0.060 mm, and the width was 10 to 11 mm.

2.3.11. Advanced rheometry

Rheometry involves characterisation and evaluation of the flow behaviour and deformation of a fluid material. A rheometer is an instrument used to investigate the viscoelastic properties of various materials, including polymer solutions, food products, coatings, inks, etc [28]. It measures the stress-strain relationship to understand how a material flows or deforms under applied forces. The rheological properties and viscosity measurements are commonly done using techniques that fall into three main categories. The rotational method estimates viscosity from the torque and rotational speed of a spindle or rotor immersed in the fluid material. The capillary method determines viscosity by measuring the fluid's flow rate and the pressure drop across a capillary tube. Lastly, the falling or rolling ball method estimates viscosity by recording the time it takes for a ball of known density to travel a certain distance through the test fluid [29].

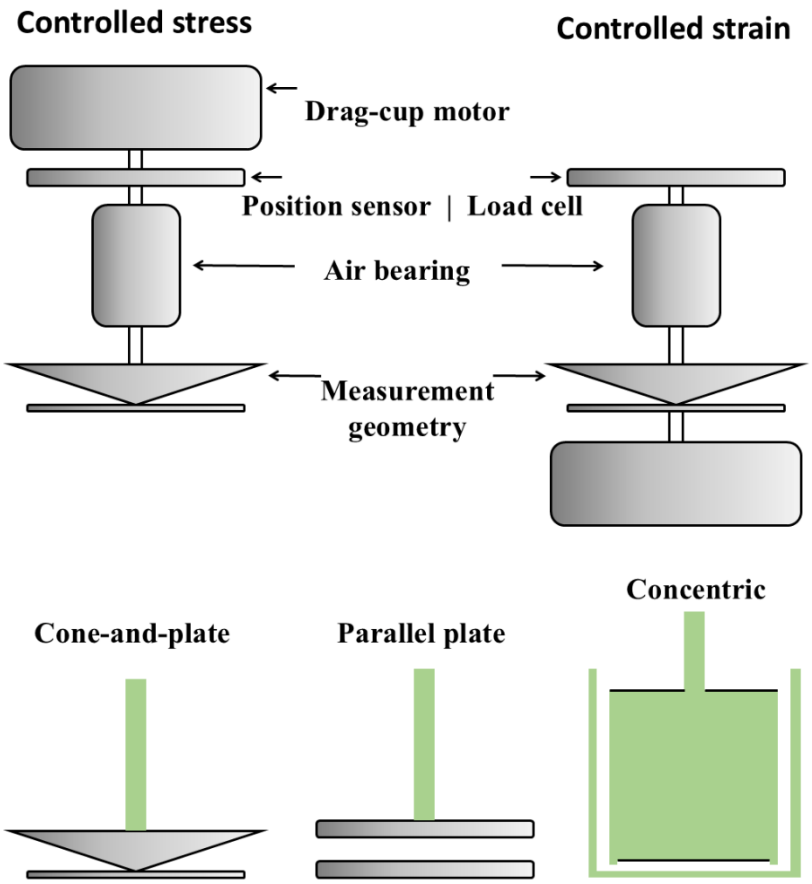

Figure 2.4: The schematic representation shows two types of rotary rheometers, along with their common measuring geometries.

Most rheometers share similar measurement geometries, such as parallel plate, cone-and-plate, or concentric cylinder set-ups and operate within a comparable range (Fig. 2.4) [30]. However, the operating principles may vary between instruments, incorporating techniques like rotation, relaxation, creep, oscillation, etc. It is primarily used to uncover the nonlinear viscoelastic behaviour of materials in flow, analyze the relationship between applied stress and structural deformation, and uncover related physical and chemical properties. While fluids flow at specific rates, solids can undergo deformation to a certain degree. The fundamental law relating to the flow behaviour of an ideal liquid,

$$\tau = \eta . \dot{\gamma} \tag{2.9}$$

where τ is the shear stress, η is the viscosity, and $\dot{\gamma}$ is the shear rate of the fluid. For a shear-thinning fluid, the relationship between shear stress (τ) and shear rate ($\dot{\gamma}$) can be plotted on log–log coordinates and is estimated by a straight line for varying shear rates, given by the equation,

$$\tau = K.\dot{\gamma}^{m} \tag{2.10}$$

and, in relations of the apparent viscosity, it is represented as,

$$\eta = K.\dot{\gamma}^{m-1} \tag{2.11}$$

When $0 < m < 1$, it results in $d\eta = d\dot{\gamma} < 0$, indicating shear-thinning behaviour in fluids. This means that shear-thinning is characterized by a power-law index m, which is less than unity. The smaller the value of m, the more pronounced the shear-thinning property is. The other parameter, K, is the consistency index, which represents the fluid consistency of a material. Equation 2.10 describes the power-law model, which applies to non-Newtonian fluids that do not exhibit yield stress. When m=1, the fluid behaves as a Newtonian fluid. If $m > 1$, the fluid exhibits shear-thickening (dilatant) behaviour, while $m < 1$ indicates shear-thinning behaviour. Both dilatant and shear-thinning types are kept under the category of non-Newtonian fluids.

The most commonly used rheological techniques employ rotational instruments to examine the behaviour of a material under various conditions, which can operate under either stress-controlled or rate-controlled modes. A rotational rheometer typically comprises four key components: the measuring geometry, a mechanism for applying shear stress or rotational speed to the sample, a sensor to detect the response of a sample, and a highly accurate temperature control system to maintain consistent testing conditions.

The rheological behaviour of the prepared fluids is investigated using an Anton Paar MCR702 rheometer and a cone plate measuring geometry (CP50-1).

2.4 Processing of WSe_2 and WS_2 dispersed NaCMC polymeric nanocomposites

2.4.1 Processing of WSe_2/NaCMC nanocomposites

WSe_2/NaCMC nanocomposite solutions were prepared using the solution-evaporation method, and their rheological behaviour was studied and discussed in the subsequent section, specifically at 1 wt.% WSe_2 loadings. In this regard, carboxymethyl cellulose was chosen as the host matrix. Specifically, the sodium salt form of carboxymethyl cellulose (NaCMC), known for its high viscosity, extra purity and biocompatibility, was preferred and procured from LOBA CHEMIE PVT. LTD., through the local supplier (Zenith India®). Cellulose and its derivatives are widely recognized for their environmentally

friendly nature, excellent film-forming capabilities, biodegradability, and low toxicity [31].

At first, a 1% NaCMC stock solution was made by dissolving 0.5 g of NaCMC powder in 50 mL of deionized (DI) water. This solution was placed on a magnetic stirrer and stirred at ~1000 RPM for ~1 h at a temperature of 70°C. Then, 1 wt.% nanocomposite solution was prepared by dispersing 5 mg of un-irradiated, exfoliated WSe_2 powder into 50 mL of a 1% NaCMC stock solution. The solution was then stirred continuously for more than 24 h at ~1200 RPM and 60 °C to attain a homogeneous solution. In addition, WSe_2 samples with similar concentration were prepared and irradiated with γ-rays at doses of 10 kGy and 35 kGy to study the effect of radiation on their fluid behaviour.

2.4.2 Processing of WS_2/NaCMC nanocomposites

The tensile properties of the 2D layered WS_2 system are discussed in Chapter 3, for which thin films were prepared by dispersing the material into a polymer solution to form WS_2/NaCMC nanocomposites. The WS_2/NaCMC nanocomposite films were prepared using the solution casting method with varying concentrations of 0.5, 1, and 5 wt.%. Initially, a 1% NaCMC stock solution was made by dissolving 0.5 g of NaCMC powder in 50 mL of deionized (DI) water. This solution was placed on a magnetic stirrer and stirred at ~1000 RPM for ~1 h at a temperature of 70°C. Subsequently, nanocomposite solutions were prepared with different wt.% of WS_2/NaCMC composites, calculated using a specific formula:

$$x\,\% = \frac{w_d}{w_d + w_p} \times 100 \tag{2.12}$$

Here, w_d is the weight of WS_2 content, and w_p is the weight of the required NaCMC polymer. Initially, a 0.5 wt.% composite system was prepared by dispersing 2.5 mg of un-irradiated, exfoliated WS_2 powder into 50 mL of a 1% NaCMC stock solution. The solution was then stirred continuously for ~24 h at ~1000 RPM and 60 °C to attain a homogeneous solution. Following the same process, 1 wt.% and 5 wt.% composite solutions were then prepared. The NaCMC solutions, containing varying amounts of WS_2, were poured separately into borosilicate glass petri dishes and oven-dried at 50 °C to form films. The schematic representation of solution-casted films for pure NaCMC and different concentrations of WS_2 contents is shown in Fig. 2.5. Once dried, the films were peeled off

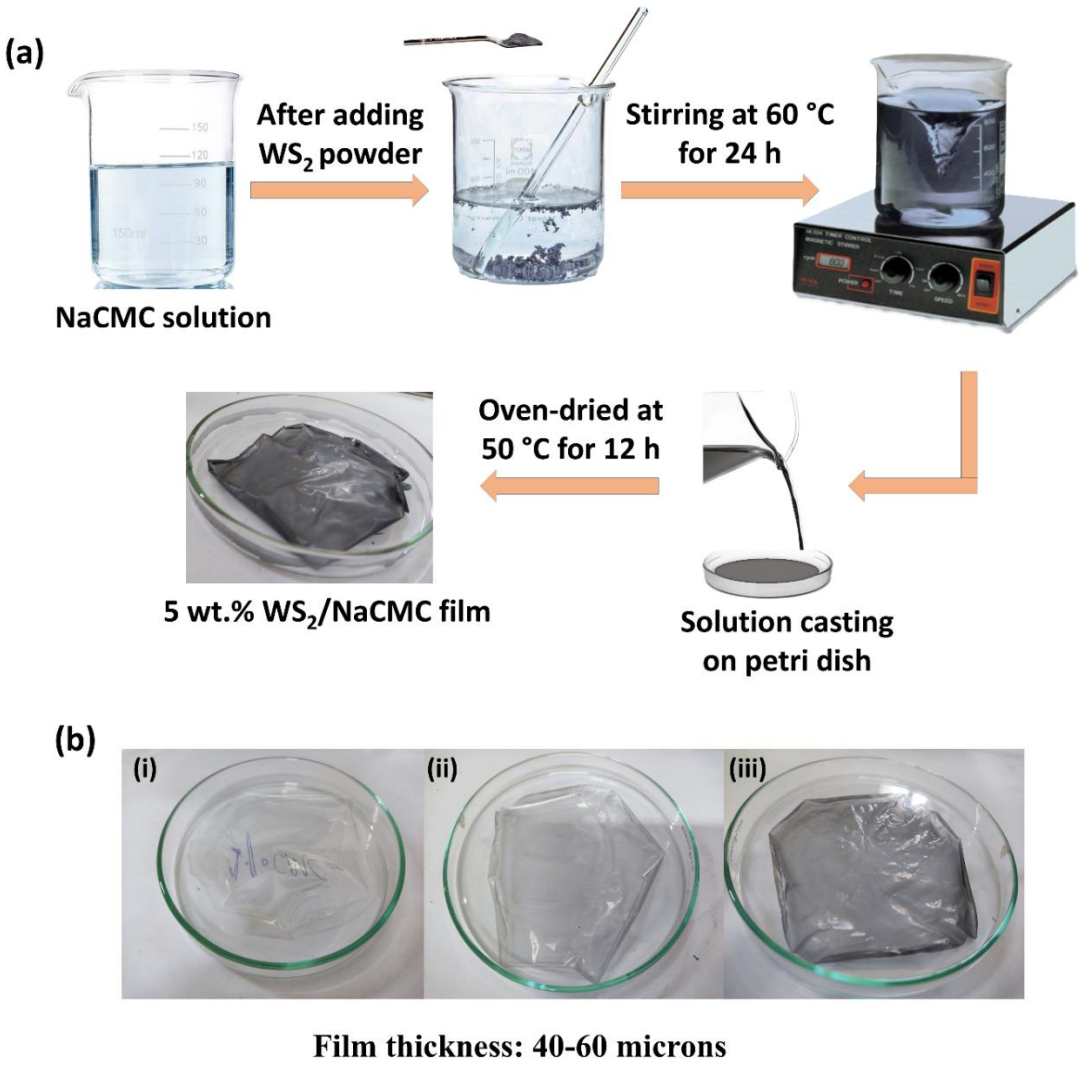

Figure 2.5: (a) Schematic representation of solution-casted films, (b) digital images of films made up of (i) NaCMC, and with varied concentrations of WS_2 content, i.e. (ii) 0.5, (iii) 1 wt.% WS_2/NaCMC films.

and used for tensile measurements. Additionally, WS_2 samples with similar concentrations were prepared and subjected to radiation at specific doses to explore the effects of radiation doses on the tensile characteristics.

2.4.3 Generating fractal patterns in NaCMC dispersed with 2D layer WS_2 system

The formation of patterns in micro- and nano-structures, resulting from the crystal growth of various polymer blends or polymer-based composites under non-equilibrium crystallization conditions, has attracted significant interest in condensed matter research [32]. The mechanisms of pattern formations are primarily governed by growth kinetics at the substrate surface, instability factor, particle transport phenomena, and boundary

conditions such as surface energy density, anisotropy effect, supercooling, and diffusivity [33]. Fractal geometry provides a useful concept to simplify and interpret many complex, disordered growth processes, and help manifest structure-property relation of the material. Furthermore, precise control over the growth of such 2D fractal patterns paves the way for the development of next-generation, low-dimensional nanomaterial-based artificial intelligence devices.

Fractal-like patterns were observed at different concentrations as WS_2/NaCMC nanocomposites were prepared and drop-casted onto glass substrates. These structures were broadly characterized and are discussed in detail in the following sections.

2.4.3.1 X-ray diffraction analysis

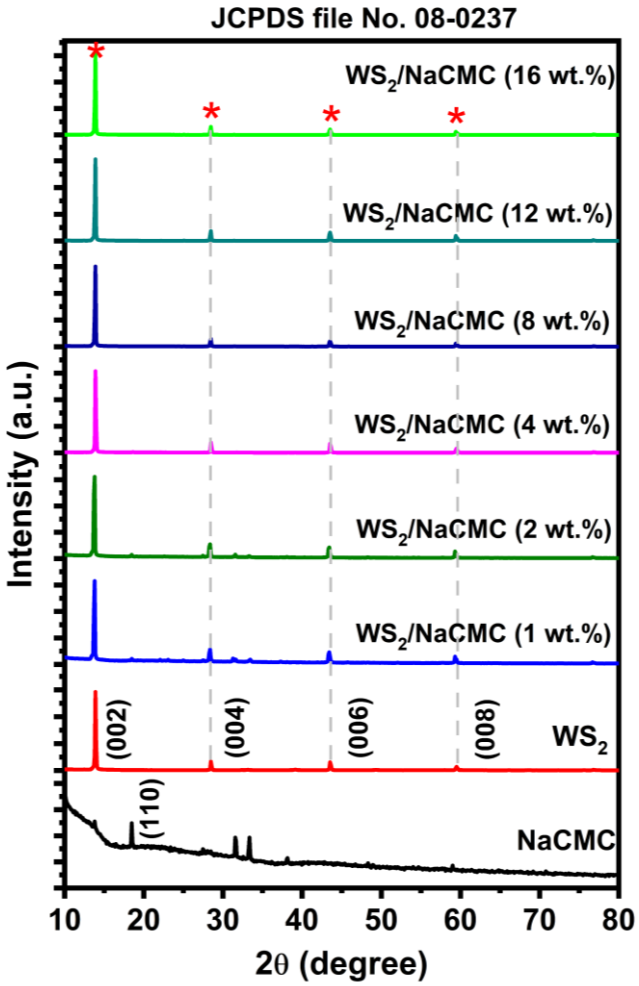

Figure 2.6: The powder XRD patterns of NaCMC, WS_2 and WS_2/NaCMC composites are shown. The NaCMC shows an amorphous and low crystalline nature, whereas WS_2 and WS_2/NaCMC composites are indexed to the hexagonal crystal structure of space group *P63/mmc.*

The crystalline structures of NaCMC, WS_2 nanosheets, and WS_2/NaCMC composite films with varying concentrations (1, 2, 4, 8, 12, and 16 wt.%) were analyzed using X-ray diffraction (XRD). The measurements were performed with a CuK_α radiation source (λ = 1.543 Å), as illustrated in Fig. 2.6. The NaCMC exhibited characteristic diffraction peaks within the 2θ range of 10º to 80º, specifically at ~18.48º, 31.66º, and 33.36º. Here, the peak at ~18.48º in the NaCMC corresponded to the (110) plane. These peaks suggest the polymer matrix possesses both amorphous and low-crystalline characteristics [34]. In contrast, the diffraction patterns of WS_2 and the WS_2/NaCMC composites showed peaks at 2θ values of around 13.90º, 28.37º, 43.44º, and 59.41º, corresponding to the (002), (004), (006), and (008) planes of the hexagonal crystal structure. These planes are indexed to the *P63/mmc*, space group (No. 194) according to JCPDS file No. 08-237 [35]. The (002) peak is particularly intense, indicating a preferred orientation of WS_2 crystallites along the *c*-axis. The presence of additional WS_2 peaks in the composite films suggests that their crystalline nature remains preserved even when dispersed within the NaCMC matrix. However, the inherent crystallinity of NaCMC appears to be significantly diminished upon incorporation of WS_2 nanosheets.

2.4.3.2 Raman vibrational modes

The Raman spectra of WS_2/NaCMC nanocomposites with WS_2 loadings ranging from 4 wt.% to 16 wt.%, each fitted with multi-peak Lorentzian curves, are represented in Fig. 2.7 (a). The two primary first-order optical phonon modes, E^1_{2g} (in-plane vibration) and A_{1g} (out-of-plane vibration) at the Γ point of the Brillouin zone are observed at ~350 cm^{-1} and 418 cm^{-1}, respectively. Additionally, at higher concentrations of WS_2/NaCMC nanocomposites, the 2*LA* mode appears at ~338 cm^{-1} [36]. The intensity ratios of the E^1_{2g} to A_{1g} modes were considered for samples with 1 wt.%, 2 wt.%, 4 wt.%, 8 wt.%, 12 wt.%, and 16 wt.% WS_2, as well as for pure WS_2 (without NaCMC). These ratios display a non-linear increase with higher WS_2 content, as shown in Fig. 2.7 (b). Furthermore, the individual intensities of both E^1_{2g} and A_{1g} modes also increase disproportionately with increasing WS_2 concentration in the dispersion state, as illustrated in Fig. 2.7 (c). The distinct E^1_{2g} and A_{1g} modes appeared indistinguishable, due to the limited amount of WS_2 dispersed within the NaCMC matrix at lower concentrations of WS_2 loadings (specifically 1 wt.% and 2 wt.%). According to the literature, the E^1_{2g} mode is highly sensitive to uniaxial strain, whereas the A_{1g} mode remains largely unaffected by strain. Conversely, doping can alter the A_{1g} vibrational mode without significantly impacting the E^1_{2g} mode

[37]. In light of this, and considering that our system involves layered structures with fractal like patterns, we propose three possible reasons: (i) a disproportionate increase in E^1_{2g} mode intensity, (ii) a disproportionate increase in A_{1g} mode intensity, and (iii) a simultaneous increase in both E^1_{2g} and A_{1g} mode intensities with increasing WS_2 content. While the first two scenarios may occur independently, the first and third possibilities are more applicable to our observations, owing to the apparent structural evolution of WS_2 in the dispersion state. When dispersed within the NaCMC matrix, the in-plane vibrations of WS_2 are possibly suppressed due to the confined environment, and the exfoliated WS_2 sheets may undergo surface modifications at their active sites at the edges.

This interaction allows the high surface area of WS_2 to effectively engage with the cellulose environment, facilitating the removal of dangling bonds. As a result, the intensity of the E^1_{2g} mode significantly decreases at a loading of 1 wt.%, while the A_{1g} mode remains largely unaffected by the strain induced by cellulose encapsulation. Furthermore, the WS_2

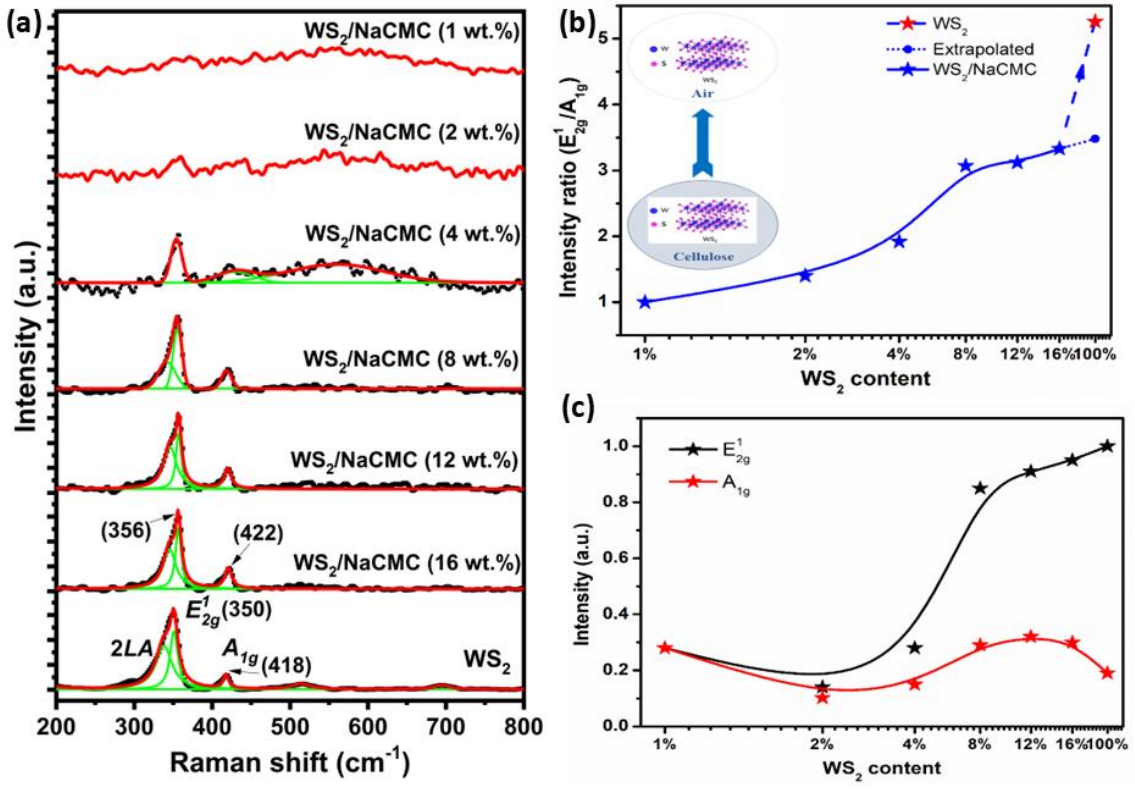

Figure 2.7: (a) Raman spectra of WS_2 and WS_2/NaCMC nanocomposite systems for different loading cases with deconvoluted multipeak Lorentzian fitting for each spectra up to 4 wt.%, (b) the trend of E^1_{2g}-to-A_{1g} mode intensity ratio with loading is plotted to illustrate the role of the host matrix, (c) The non-linear trend for definite intensities of E^1_{2g} and A_{1g} modes can be found with increasing content of WS_2.

Table 2.1. The peak positions of Raman modes, line widths and the intensities were estimated through the acquired Raman spectra.

Sl. No.	Sample	E^1_{2g} mode (cm^{-1})	A_{1g} mode (cm^{-1})	Line width		Intensity		E^1_{2g} -to-A_{1g} intensity ratio
				E^1_{2g} mode (cm^{-1})	A_{1g} mode (cm^{-1})	E^1_{2g} mode	A_{1g} mode	
1	WS_2	350	418	11.8	8.4	1.0	0.2	5.3
2	16 wt.% WS_2/NaCMC	356	420	10.8	12.6	1.0	0.3	3.2
3	12 wt.% WS_2/NaCMC	356	420	7.7	8.9	1.0	0.3	3.0
4	8 wt.% WS_2/NaCMC	356	420	17.0	10.6	0.8	0.3	2.9
5	4 wt.% WS_2/NaCMC	354	426	16.1	34.1	0.3	0.2	1.9

concentration, ranging from 1 wt.% to 100 wt.%, against the E^1_{2g}-to-A_{1g} intensity ratio derived from the Raman spectra was plotted as shown in Fig. 2.7 (b) and listed in Table 2.1. Interestingly, with increasing WS_2 content, the nonlinear trend shifts sharply upward, indicating that WS_2 structures are now in a less dispersed state and a lesser amount is accessible to the cellulose matrix.

2.4.3.3 FT-IR spectra

The FT-IR spectra of pure NaCMC, WS_2 nanosheets, and WS_2/NaCMC nanocomposites at various concentrations (1, 2, 4, 8, 12, and 16 wt.%) are shown in Fig. 2.8. In the NaCMC curve, the band around ~614 cm^{-1} corresponds to C–H bending vibrations of alkyne groups [38]. The absorption bands at ~1032 cm^{-1} and 1107 cm^{-1} are attributed to aromatic C–H in-plane bending vibrations, consistent with previous reports [39]. Moreover, the peaks located at ~1618 cm^{-1}, 1328 cm^{-1}, and 3412 cm^{-1} are associated with the carboxylate group, OH in-plane bending, and hydrogen-bonded OH stretching vibrations, respectively [40]. For the WS_2 case, bands observed around 492 cm^{-1} and 941 cm^{-1} are assigned to S–S

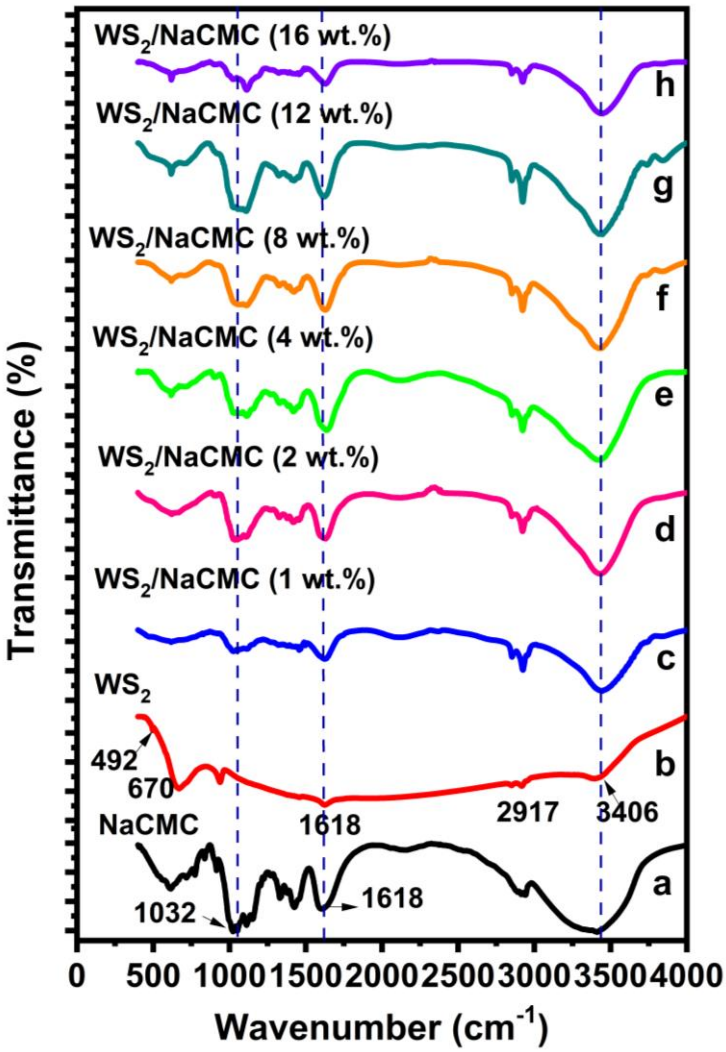

Figure 2.8: FT-IR spectra of (a) NaCMC, (b) WS_2, (c) 1 wt.% WS_2/NaCMC, (d) 2 wt.% WS_2/NaCMC, (e) 4 wt.% WS_2/NaCMC, (f) 8 wt.% WS_2/NaCMC, (g) 12 wt.% WS_2/NaCMC, and (h) 16 wt.% WS_2/NaCMC. Note that the S−S stretching and W−S stretching, and bending vibrations occur upon incorporation of WS_2 into the host cellulose.

stretching vibrations [41], while peaks about 670 cm^{-1}, 1458 cm^{-1}, 1618 cm^{-1}, and 2917 cm^{-1} correspond to W–S stretching and bending vibrations, in agreement with earlier studies [42]. Furthermore, in the WS_2/NaCMC composites, characteristic bands from both WS_2 and NaCMC are evident across all the concentrations considered, with noticeable broadening and slight shifts in peak positions, due to the interactions among the IR-active molecules [43].

The positions of bands in the IR spectra are largely influenced by the relative atomic masses, force constants of the bond between atoms, and their structural arrangement. The prediction of molecular vibrations, based on a simplified Hooke's law, assumes the vibrational frequency or wavenumber ($\bar{\nu}$) through the following equation [44],

Table 2.2. Stretching and bending vibrations identified from the FT-IR spectra of the WS_2 system.

Sl. No.	Bonds of WS_2	Wavenumber $\times 10^2$ (m^{-1})	Force constant (N/m)	Nature of vibration	References
1	S−S	492	229	Stretching	[39]
2	S−S	941	838	Stretching	[41]
3	W−S	670	727	Stretching	[42]
4	W−S	1458	3442	Bending	[41]
5	W−S	1618	4222	Bending	[42]

$$\bar{\nu} = \frac{1}{2\pi c}\left(\frac{f}{\frac{m_A m_B}{m_A + m_B}}\right)^{1/2}, \tag{2.12}$$

where f denotes the force constant, c is the speed of light, and m_A and m_B are the masses of atoms A and B, respectively. Using the vibrational frequencies obtained from the FT-IR spectra, the force constants for the W–S and S–S bonds were calculated based on equation (2.12) and are summarized in Table 2.2. It was found that W–S bonds are ~5 to 15 times stiffer than S–S bonds, corresponding to the stretching and bending vibrations within the system. Additionally, we observe that the S–S peaks completely disappear in the composite system, while the high-frequency W–S bending modes become broadened. Consequently, the calculation of force constants was confined to exfoliated WS_2 only.

2.4.3.4 Morphological characteristics through FE-SEM

The surface morphology of WS_2/NaCMC composites featuring fractal-like patterns was analyzed for 1–4 wt.% of WS_2 loading, as shown in Fig. 2.9 (a-h). Interestingly, the cellulose-based inorganic complexes of WS_2/NaCMC exhibit “columnar fibril” and “fractal-like” self-assembly patterns, characteristic of self-affine structures governed by anisotropic fractal scaling [45]. The fractal aggregation of particles appears to be dependent on the deposits on the glass substrates, where the growth might initiate from the edge of the air-water interfaces of the particles deposited [46]. Growth at these interfaces

is presumed to be primarily driven by capillary forces acting between the dispersed colloidal particles. Previous studies have indicated that substrate-adsorbate interactions also significantly influence such growth formations [47].

For the 1 wt.% solution, which was processed over 48 h, we observe the formation of flat, longitudinal patterns that are well-separated and aligned in specific directions (Fig. 2.9 (a, e)). In contrast, the 1 wt.% solution, processed for only 24 h results in finer self-

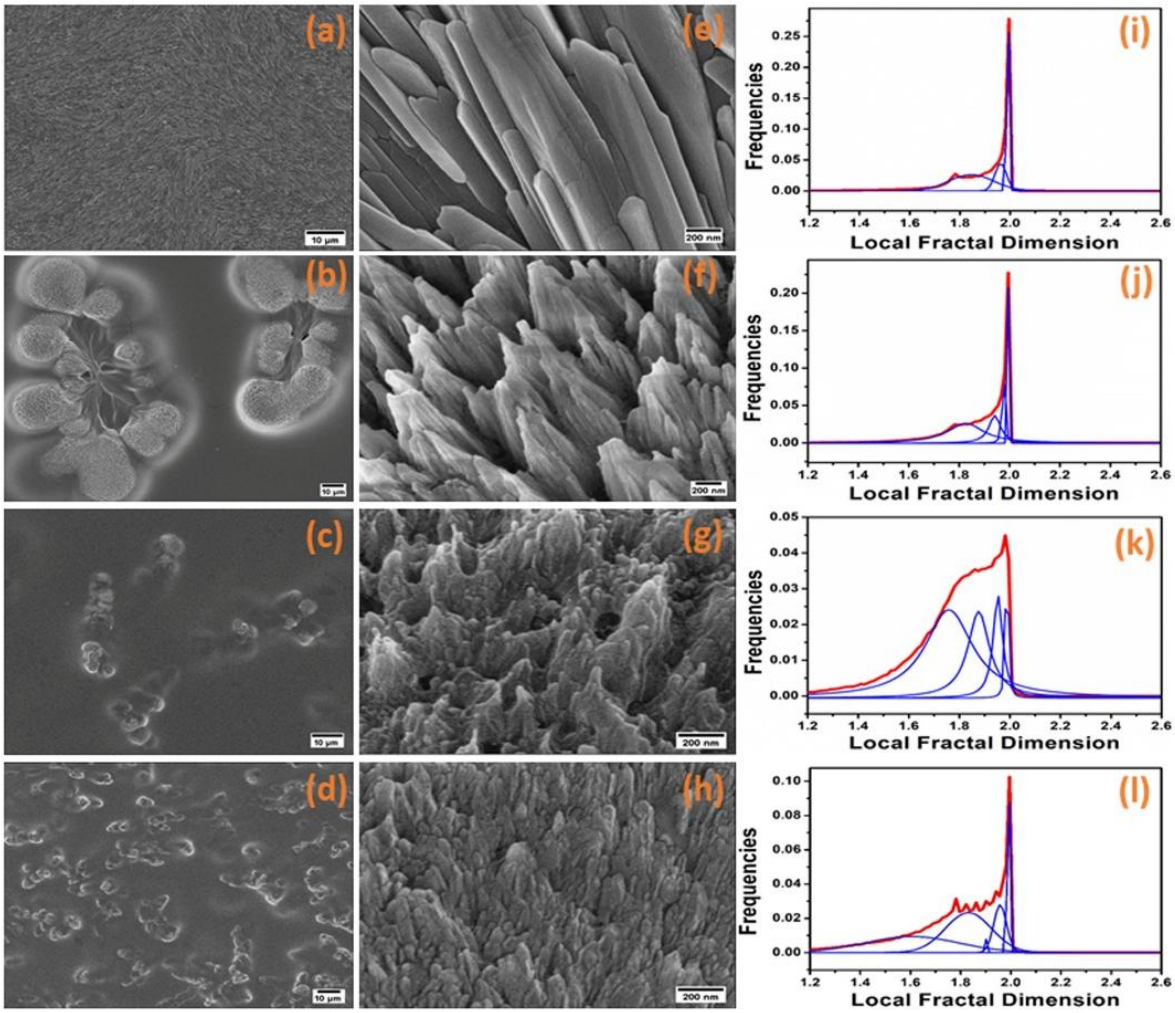

Figure 2.9: (a-d) correspond to FE-SEM images for WS_2/NaCMC nanocomposites at lower magnifications (scale bar: 10 µm), whereas (e-h) represent magnified images (scale bar: 200 nm) of the systems under study. The images were captured for (a,e) 1 wt.% (48 h), (b,f) 1 wt.% (24 h), (c,g) 2 wt.% (48 h), and (d,h) 4 wt.% (48 h), respectively. (i-l) shows the multi-peak Lorentzian fits of local fractal dimension *vs.* frequency plots for each specimen.

aggregated structures interspersed with pockets of discontinuous phase, likely due to the abrupt incorporation of NaCMC into WS_2 layers under vigorous stirring, as seen in Fig. 2.9 (b, f). Lower-magnification micrographs highlight the broader effects of the dispersing agents, while higher-magnification images reveal more intricate self-organized patterns. At these higher magnifications, the structures resemble fractal or termite-like formations, with greater void presence in the lower WS_2 content. Notably, NaCMC acted not merely as a dispersant but also actively percolated through specific local sites of the WS_2 flakes.

The viscous flow of NaCMC into the WS_2 flakes, with occasional confinement, is expected to disrupt the weak van der Waals bonds under agitation. Rather than following a typical diffusion-limited aggregation (DLA) mechanism, we propose that the flakes undergo a site-specific percolation-driven disruption by NaCMC, a process termed as diffusion-limited disruption (DLD) [48]. This phenomenon is particularly evident in the 2 wt.% and 4 wt.% WS_2 loading cases (Fig. 2.9 (c, g) and (d, h)). It is important to note that, in DLA, particle aggregation occurs through random walks induced by thermal agitation [49]. In contrast, in the present case, NaCMC appears to be surface-adsorbed onto the stacked WS_2 layers. The resulting patterns for the 2 wt.% and 4 wt.% samples are distinctly different, suggesting that repulsive interactions between individual units may arise, likely due to a screening effect strongly influenced by the rate of diffusion [50]. Previous studies have also indicated that the self-assembly of such composites is sensitive to growth conditions, such as factors like solvent evaporation temperature, drying rate, solute concentration, and the nature of the substrate used for film casting.

Fractal analysis: The dimensions of surface textures can be assessed by employing fractal analysis techniques [51]. Fractal dimensions, often referred to as the Hausdorff-Besicovitch dimensions, are used to characterize rough, fragmented, or irregular surfaces. The box-counting method is commonly employed to estimate these dimensions from well-resolved images, regardless of whether they exhibit self-similarity or not [52]. In this study, FE-SEM images were converted into binary images using the box-counting method via the ImageJ® 1.53e software (with the FracLac plugin) [53]. This method involves overlaying the image with grids of boxes and determining the number of boxes needed to fully cover the structures within the image. If the box size is denoted by $\mathcal{E}$ and the corresponding number of boxes required by $N(\mathcal{E})$, the fractal dimension can then be calculated using the following relationship [54],

$$N(\varepsilon) \propto \varepsilon^{-d_f}, \tag{2.13}$$

where d_f is the fractal dimension. Considering the logarithm of equation (2.13),

$$ln\ N(\varepsilon) = d_f\ ln\ (\frac{1}{\varepsilon}) + \text{constant}, \tag{2.14a}$$

and accordingly,

$$\lim_{\varepsilon \to 0} \frac{\ln N(\varepsilon)}{\ln (1/\varepsilon)} = d_f \tag{2.14b}$$

The fractal dimension (d_f) is determined from the slope of the ln $N(\varepsilon)$ vs. $ln\ (1/\varepsilon)$ plot, derived from the corresponding regression equation. Local fractal dimension vs. frequency plots, along with multi-peak Lorentzian fits exhibiting the highest correlation values, are shown adjacent to the FE-SEM micrographs on the right side of Fig. 2.9 (i-l).

In all cases, besides the prominent peak at $d_f \approx 2$, bimodal and trimodal self-similar patterns are revealed after deconvolution. These plots exhibit asymmetric broadening, with shoulder peak maxima ranging from ~1.93 to 1.6. This suggests that fractal-like structures are embedded within the underlying 2D WS_2 surface. A decrease in the fractal dimension with increasing WS_2 content is attributed to the loss of finer structural elements from the self-similar patterns, driven by the infiltration of NaCMC into the WS_2 flakes. While the 2D geometry is preserved, the emergence of new fractal structures is facilitated by the capillary action of cellulose penetrating through interfaces and voids available. It is important to note that magnified surface images do not necessarily exhibit self-similarity across the entire structure. Nevertheless, the WS_2 material, originally a 2D structure adhering to Euclidean geometry, exhibits localized reductions in dimensionality, generating fractal patterns with dimensions ranging from ~1.6 to 1.98, as detailed in the *Appendix* (Table A1).

2.4.3.5 Surface morphology through AFM

The 3D topography and 2D surface scans of the WS_2/NaCMC composite films, specifically at 1 wt.% and 4 wt.% loadings, captured at selected sites are presented in Fig. 2.10 (a-f). AFM scans, covering areas of 10×10 μm^2 and 2.5×2.5 μm^2, were performed in semi-contact mode using a silicon probe with an approximate tip diameter of ~10 nm, positioned 14-16 μm above the sample surface. All micrographs were analyzed using WSxM 5.0 Develop 10.1 software (Nanotec, Inc.), which enabled detailed evaluation of

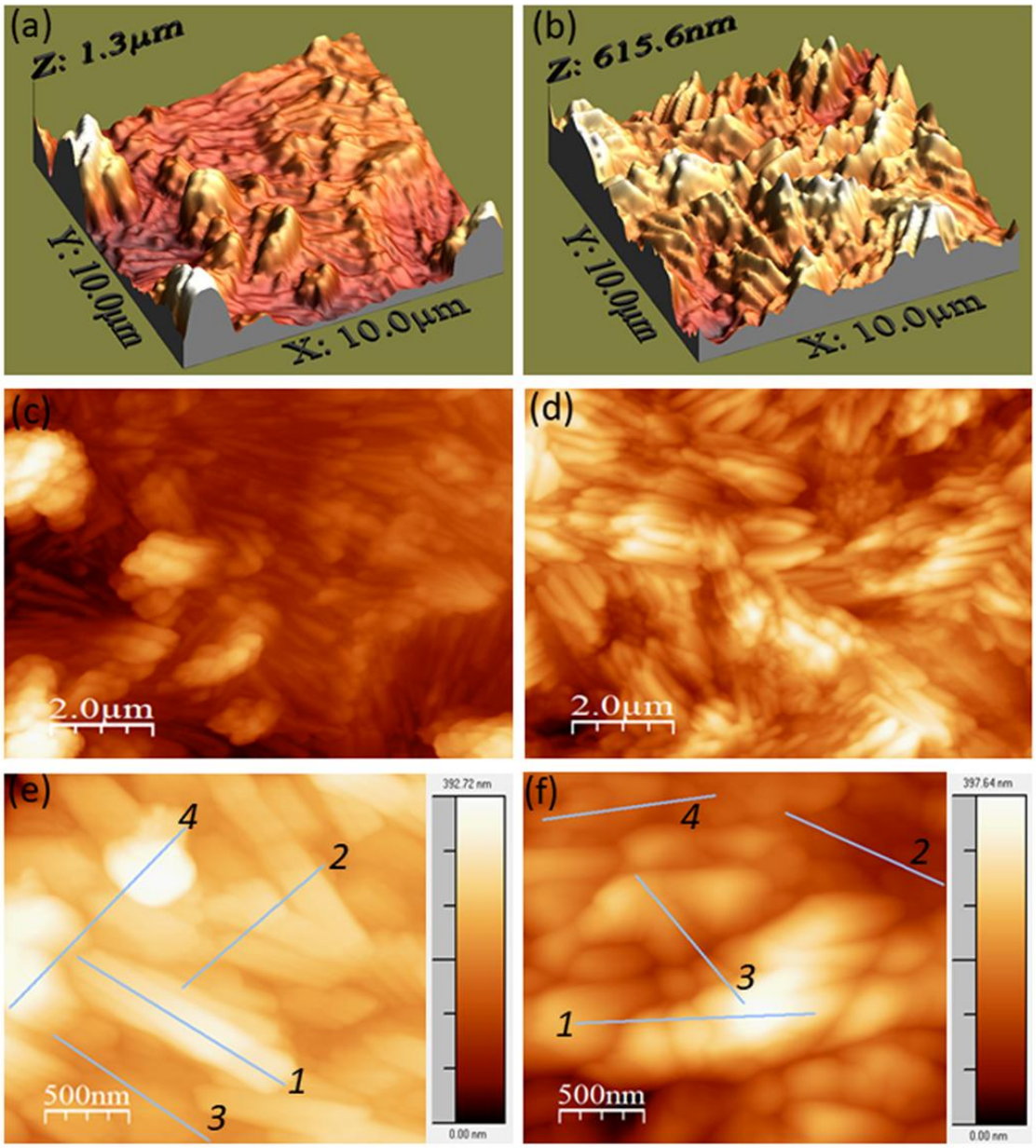

Figure 2.10: AFM of (a,b) 3D topography and (c,d) 2D surface scan images for 1 wt.% and 4 wt.% WS_2/NaCMC nanocomposites can be found. Note the nature of conical bumps and voids that exist in each image. (e,f) shows the magnified 2D views of 1 wt.% and 4 wt.% WS_2/NaCMC nanocomposites with selected sites for directional scanning. The sites are being designated with italic font numerals, *1,2,3,* etc.

height profiles and root-mean-square (RMS) roughness values [55]. Morphologically, the 2D AFM images closely resemble the structures observed in the FE-SEM images discussed earlier. The surface topography reveals self-similar oblates and pockets, with the characteristic appearance of fractal-like aggregates. Notably, finer structures are more

Table 2.3. RMS roughness, skewness and kurtosis obtained from the AFM analysis.

Sl. No.	RMS roughness (nm)	Skewness	Kurtosis
1	45.1 ± 6.02	- 0.2024	5.8336
2	66.5 ± 15.03	0.5463	3.5675

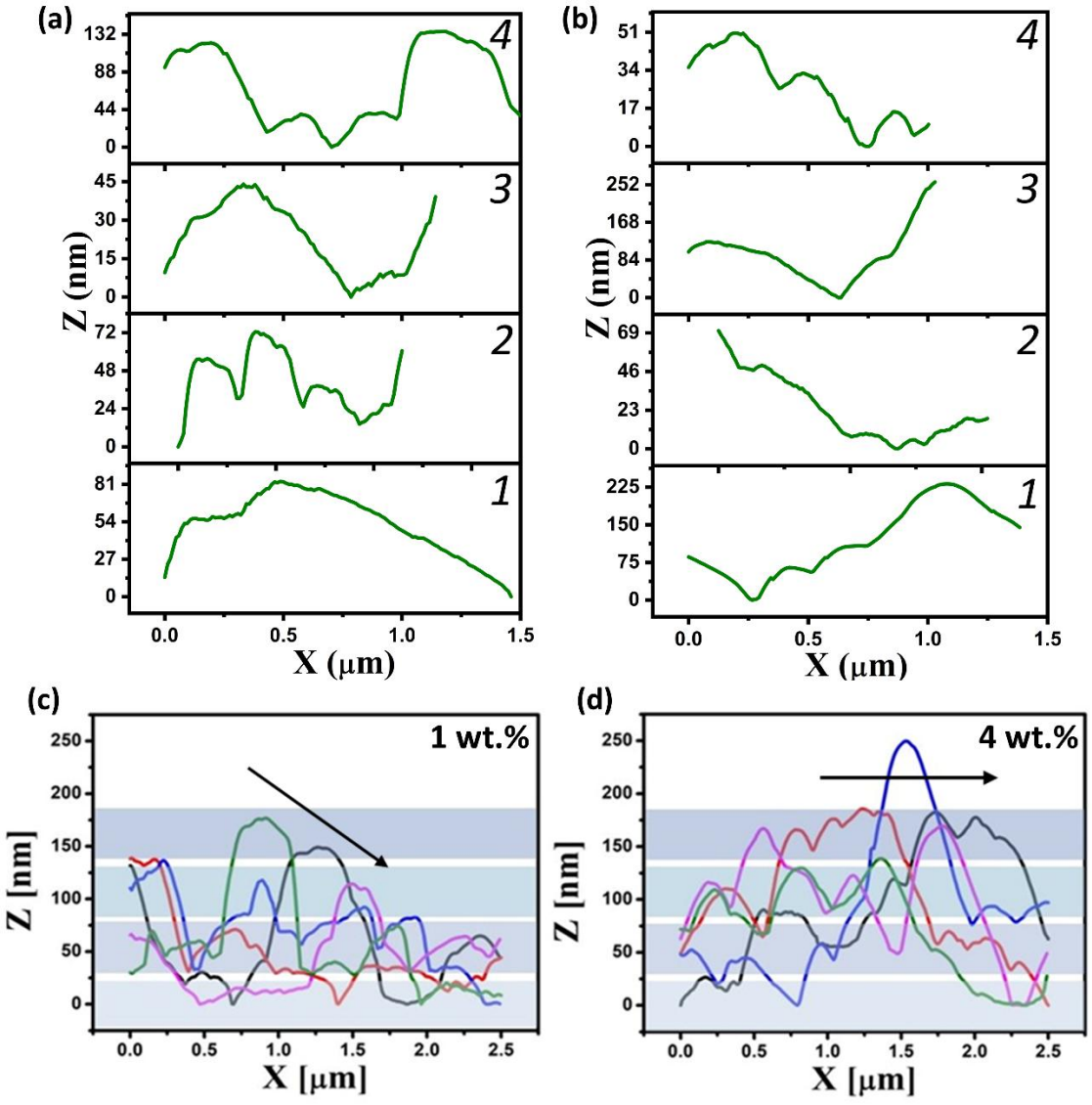

Figure 2.11: (a) Directional height profiles considered along the marked lines for 1 wt.%, and (b) for 4 wt.% WS_2/NaCMC nanocomposites already featured in Fig. 2.10 (e,f). Here, (c,d) height profiles of horizontal line scans are obtained from 5 specific regions, and the arrowhead lines essentially depict the variation of height over distances in the specimen from the left.

evident in the 4 wt.% WS_2/NaCMC films compared to those with 1 wt.% loading. The 3D imaging offered nanohillocks, gradient-valleys and pockets in isolation from each other.

Widely utilized in the study of growth phenomena, surface roughness is a critical parameter, typically expressed as the root-mean-square (RMS) roughness [56],

$$\sigma = \sqrt{\langle [h(\boldsymbol{r},t) - \langle h(\boldsymbol{r},t)\rangle]^2\rangle} \tag{2.15}$$

It is also referred to as the interface width, which characterizes the surface height profile $h(r)$. The 4 wt.% WS_2/NaCMC sample exhibits a higher surface roughness ($\sigma \approx 66.5 \pm 15.03$ nm) compared to the 1 wt.% sample ($\sigma \approx 45.1 \pm 6.02$ nm), as shown in Fig. 2.10 and Table 2.3.

Additionally, to gain more detailed information about the surface, the parameters such as skewness (which compares peaks to valleys) and kurtosis (which reflects the density and sharpness of peaks) in the height distribution are examined [57]. The 1 wt.% specimen shows negative skewness, indicating a surface dominated by valleys or holes. In contrast, the 4 wt.% sample exhibits positive skewness, suggesting a surface with asperities, bumps or spikes. Both surfaces display leptokurtic distributions, characterized by sharp peaks and flatter features, consistent with their high kurtosis values which is greater than 3.

The scanning analysis was made independently along the lateral direction of individual rods, passing through multiple grains and voids. Four independent scans were obtained for each system considered, as shown in Fig. 2.11 (a, b). The elongated structures appear smooth along their lengths, whereas numerous bumps are observed across the grains. The numerals 1, 2, 3, etc., marked in Fig. 2.10 (e, f), correspond to the scanned lengths highlighted in Fig. 2.11 (a, b). Additionally, height profiles from five horizontal line scans taken from different regions are presented in Fig. 2.11 (c, d). Overall, a gradient in surface roughness is evident in the 1 wt.% WS_2/NaCMC sample. It is important to note that rough surfaces cannot be fully characterized by a single dimension. Nevertheless, the emergence of fractal geometries, as previously anticipated, supports the observed roughness patterns in the WS_2/NaCMC composites under investigation.

2.5 Concluding remarks

In conclusion, the synthesis routes and the characterization techniques that are involved in this thesis work are detailed in this chapter. Moreover, the formation of fractal-like patterns of WS_2/NaCMC composites grown via the solvent-evaporation route, with analysis carried out by various characterization techniques, is discussed. The morphological evolution of fractal structures was evident from both FE-SEM and AFM imaging analysis. Here, NaCMC acted as a host matrix as well as a percolating agent, thus playing an important role in the pattern formation in the 2D WS_2 system. The fractal dimension *vs.* frequency curves were plotted by analyzing the FE-SEM images through the box counting method, where we could notice locally connected fractal dimensions with the appearance of bi- and tri-modal fractal features in the background of a 2D WS_2 system. The dimensions were seen to be varied from 1.98 to 1.60 with increasing WS_2 content (1-4 wt.%) in the composites. Thus, by taking advantage of the concepts of exfoliation and percolation, 2D transitional fractals (with dimensions below 2) developed hold great potential for applications in smart sensors, flexible electronics, wearable units and many more.

References

[1] Abid, N., Khan, A.M., Shujait, S., Chaudhary, K., Ikram, M., Imran, M., Haider, J., Khan, M., Khan, Q., Maqbool, M. Synthesis of nanomaterials using various top-down and bottom-up approaches, influencing factors, advantages, and disadvantages: A review. *Advances in Colloid and Interface Science*, *300*: 102597, 2022.

[2] Shrivastava, M., Ramgopal Rao, V. A roadmap for disruptive applications and heterogeneous integration using two-dimensional materials: State-of-the-art and technological challenges. *Nano Letters*, *21*(15): 6359–6381, 2021.

[3] Agrawal, A. Top-down strategies for achieving high-quality graphene: Recent advancements. *Journal of Industrial and Engineering Chemistry*, *142*: 103–126, 2025.

[4] Geim, A. K., Novoselov, K. S. The rise of graphene. *Nature Materials*, *6*(3): 183–191, 2007.

[5] Shen, J., Wu, J., Wang, M., Dong, P., Xu, J., Li, X., Zhang, X., Yuan, J., Wang, X., Ye, M., Vajtai, R. Surface tension components based selection of cosolvents for efficient liquid phase exfoliation of 2D materials. *Small*, *12*(20): 2741–2749, 2016.

[6] Papageorgiou, D. G., Dong, M., Zhang, H., Liu, M., Young, R. J. Mechanical properties of transition metal dichalcogenides: towards high-performance polymer nanocomposites. *2D Materials*, *12*(1): 012002, 2025.

[7] Eftekhari, A. Tungsten dichalcogenides (WS_2, WSe_2, and WTe_2): materials chemistry and applications. *Journal of Materials Chemistry A*, *5*(35): 18299–18325, 2017.

[8] Epp, J. 4 - X-ray diffraction (XRD) techniques for materials characterization. In G. Hübschen, I. Altpeter, R. Tschuncky, & H.-G. Herrmann (Eds.), *Materials Characterization Using Nondestructive Evaluation (NDE) Methods*, pages 81–124, ISBN:978-0-08-100040-3, Woodhead Publishing, 2016.

[9] Sayeed, M. A. *Electrochemical fabrication of nanostructured metal oxides for the oxygen evolution reaction.* Queensland University of Technology, 2018.

[10] Cullity, B. D., Smoluchowski, R. Elements of X-ray Diffraction. *Physics Today*, *10*(3): 50, 1957.

[11] Frentrup, M., Hatui, N., Wernicke, T., Stellmach, J., Bhattacharya, A., Kneissl, M. Determination of lattice parameters, strain state and composition in semipolar III-nitrides using high resolution X-ray diffraction. *Journal of Applied Physics*, *114*(21): 2013.

[12] Tissue, B. M. Ultraviolet and visible absorption spectroscopy. *Characterization of Materials*, 2002.

[13] Borchert, H., Borchert, H. Absorption and photoluminescence spectroscopy. *Solar Cells Based on Colloidal Nanocrystals*, 196: 119–127, 2014.

[14] Li, Q., Anpo, M., You, J., Yan, T., Wang, X. Photoluminescence (PL) Spectroscopy. In *Springer Handbook of Advanced Catalyst Characterization*, pages 295–321, Springer, 2023.

[15] Paul, W. Photoluminescence. In *Physics of Structurally Disordered Solids*, pages 171–197, Springer, 1976.

[16] Sobiesierski, Z. Photoluminescence Spectroscopy. In J. F. McGlip, D. Weaire, & C. H. Patterson (Eds.), *Epioptics: Linear and Nonlinear Optical Spectroscopy of Surfaces and Interfaces*, pages 133–162, ISBN:978-3-642-79820-7, Springer Berlin Heidelberg, 1995.

[17] Vašková, H. A powerful tool for material identification: Raman spectroscopy. *Int. J. Math. Model. Methods Appl. Sci, 5*: 1205–1212, 2011.

[18] Stevie, F. A., Donley, C. L. Introduction to X-ray photoelectron spectroscopy. *Journal of Vacuum Science & Technology A*, *38*(6): 2020.

[19] Andrade, J. D. X-ray photoelectron spectroscopy (XPS). *Surface and Interfacial Aspects of Biomedical Polymers: Volume 1 Surface Chemistry and Physics*, 105–195, 1985.

[20] De Oliveira, R. R. L., Albuquerque, D. A. C., Cruz, T. G. S., Yamaji, F. M., Leite, F. L. Measurement of the nanoscale roughness by atomic force microscopy: basic principles and applications. *Atomic force microscopy-imaging, measuring and manipulating surfaces at the atomic scale*, *3*: 147–174, 2012.

[21] Zhou, W., Apkarian, R., Wang, Z. L., Joy, D. Fundamentals of Scanning Electron Microscopy (SEM). In W. Zhou & Z. L. Wang (Eds.), *Scanning Microscopy for Nanotechnology: Techniques and Applications*, pages 1–40, ISBN:978-0-387-39620-0, Springer New York, 2007.

[22] Akhtar, K., Khan, S. A., Khan, S. B., Asiri, A. M. Scanning Electron Microscopy: Principle and Applications in Nanomaterials Characterization. In S. K. Sharma (Ed.), *Handbook of Materials Characterization*, pages 113–145, ISBN:978-3-319-92955-2, Springer International Publishing, 2018.

[23] Kannan, M. Transmission electron microscope—Principle, components and applications. *A textbook on fundamentals and applications of nanotechnology*, 93–102, 2018.

[24] Pérez-Botella, E., Valencia, S., Rey, F. Zeolites in Adsorption Processes: State of the Art and Future Prospects. *Chemical Reviews*, *122*(24): 17647–17695, 2022.

[25] Sing, K. The use of nitrogen adsorption for the characterisation of porous materials. *Colloids and Surfaces A: Physicochemical and Engineering Aspects*, *187*3–9, 2001.

[26] Senthil Kumar, J., Surya, B., Arjun, V. S. Micro universal testing machine system for material property measurement of micro structure. In *AIP Conference Proceedings*, Vol. 3035, ISBN:0094-243X, AIP Publishing, 2024.

[27] Saritha, G., Iswarya, T., Keerthana, D., Baig, A. T. D. Micro universal testing machine system for material property measurement. *Materials Today: Proceedings,* 2023.

[28] Wang, Q., Shi, A., Shah, F. Rheology instruments for food quality evaluation. In *Evaluation technologies for food quality*, pages 465–490, Elsevier, 2019.

[29] Hou, Y. Y., Kassim, H. O. Instrument techniques for rheometry. *Review of scientific instruments*, *76*(10): 101101, 2005.

[30] Wang, Q., Shi, A., Shah, F. 18 - Rheology instruments for food quality evaluation. In J. Zhong & X. Wang (Eds.), *Evaluation Technologies for Food Quality*, pages 465–490, ISBN:978-0-12-814217-2, Woodhead Publishing, 2019.

[31] Yadav, M., Rhee, K. Y., Park, S. J. Synthesis and characterization of graphene oxide/carboxymethylcellulose/alginate composite blend films. *Carbohydrate polymers*, *110*: 18–25, 2014.

[32] Kaya, D., Belyi, V. A., Muthukumar, M. Pattern formation in drying droplets of polyelectrolyte and salt. *The Journal of Chemical Physics*, *133*(11): 114905, 2010.

[33] Yadav, M., Rhee, K. Y., Jung, I. H., Park, S. J. Eco-friendly synthesis, characterization and properties of a sodium carboxymethyl cellulose/graphene oxide nanocomposite film. *Cellulose*, *20*: 687–698, 2013.

[34] Kumar, B., Priyadarshi, R., Deeba, F., Kulshreshtha, A., Gaikwad, K.K., Kim, J., Kumar, A., Negi, Y.S. Nanoporous sodium carboxymethyl cellulose-g-poly (Sodium acrylate)/FeCl3 hydrogel beads: Synthesis and characterization. *Gels*, *6*(4): 49, 2020.

[35] Valappil, M. O., Anil, A., Shaijumon, M., Pillai, V. K., Alwarappan, S. A Single-Step Electrochemical Synthesis of Luminescent WS_2 Quantum Dots. *Chemistry–A European Journal*, *23*(38): 9144–9148, 2017.

[36] Berkdemir, A., Gutiérrez, H.R., Botello-Méndez, A.R., Perea-López, N., Elías, A.L., Chia, C.I., Wang, B., Crespi, V.H., López-Urías, F., Charlier, J.C., Terrones, H. Identification of individual and few layers of WS_2 using Raman Spectroscopy. *Scientific Reports, 3*: 1755, 2013.

[37] Wang, Y., Cong, C., Yang, W., Shang, J., Peimyoo, N., Chen, Y., Kang, J., Wang, J., Huang, W., Yu, T. Strain-induced direct–indirect bandgap transition and phonon modulation in monolayer WS_2. *Nano Research*, *8*: 2562–2572, 2015.

[38] Sang, Y., Zhao, Z., Zhao, M., Hao, P., Leng, Y., Liu, H. From UV to near-infrared, WS_2 nanosheet: a novel photocatalyst for full solar light spectrum photodegradation. *Advanced Materials (Deerfield Beach, Fla.)*, *27*(2): 363–369, 2014.

[39] Coates, J. Interpretation of infrared spectra, a practical approach. *Encyclopedia of analytical chemistry*, *12*: 10815–10837, 2000.

[40] Ovchinnikov, O.V., Evtukhova, A.V, Kondratenko, T. S., Smirnov, M. S., Khokhlov, V. Y., Erina, O. V. Manifestation of intermolecular interactions in FTIR spectra of methylene blue molecules. *Vibrational Spectroscopy*, *86*: 181–189, 2016.

[41] Hazarika, S. J., Mohanta, D. Inorganic fullerene-type WS_2 nanoparticles: Processing, characterization and its photocatalytic performance on malachite green. *Applied Physics A*, *123*: 1–10, 2017.

[42] Wu, J., Yue, G., Xiao, Y., Huang, M., Lin, J., Fan, L., Lan, Z., Lin, J.Y. Glucose aided preparation of tungsten sulfide/multi-wall carbon nanotube hybrid and use as counter electrode in dye-sensitized solar cells. *ACS applied materials & interfaces*, *4*(12): 6530–6536, 2012.

[43] Peng, K., Wang, H., Li, X., Wang, J., Cai, Z., Su, L., Fan, X. Emerging WS_2/montmorillonite composite nanosheets as an efficient hydrophilic photocatalyst for aqueous phase reactions. Sci. *Rep, A*, *9*(1): 16325, 2019.

[44] Dewan, N., Gupta, V., Sreenivas, K., Katiyar, R. S. Growth of amorphous TeO_x ($2 \leq x \leq 3$) thin film by radio frequency sputtering. *Journal of Applied Physics*, *101*(8): 084910, 2007.

[45] Libbrecht, K. G. The physics of snow crystals. *Reports on progress in physics*, *68*(4): 855, 2005.

[46] Yunker, P.J., Lohr, M.A., Still, T., Borodin, A., Durian, D.J. and Yodh, A.G. Effects of Particle Shape on Growth Dynamics at Edges of Evaporating. Drops of Colloidal Suspensions. *Physical Review Letters*, *110*(3): 035501, 2013.

[47] Loudet, J.C., Alsayed, A. M., Zhang, J., Yodh, A. G. Capillary interactions between anisotropic colloidal particles. *Physical Review Letters*, *94*(1): 018301, 2005.

[48] D'Souza, R. M., Margolus, N. H. Thermodynamically reversible generalization of diffusion limited aggregation. *Physical Review E*, *60*(1): 264, 1999.

[49] Beck, C., Schlogel, F., Klimontovich, Y. L. Thermodynamics of chaotic systems: An introduction. *Physics-Uspekhi*, *37*(7): 713, 1994.

[50] Zhao, Q., Qian, J., Gui, Z., An, Q., Zhu, M. Interfacial self-assembly of cellulose-based polyelectrolyte complexes: pattern formation of fractal "trees." *Soft Matter*, *6*(6): 1129–1137, 2010.

[51] Mandelbrot, B. B., Evertsz, C. J. G., Gutzwiller, M. C. *Fractals and chaos: the Mandelbrot set and beyond*, Vol. 3, Springer, 2004.

[52] Dallaeva, D., Ţălu, Ş., Stach, S., Škarvada, P., Tománek, P., Grmela, L. AFM imaging and fractal analysis of surface roughness of AlN epilayers on sapphire substrates. *Applied Surface Science*, *312*: 81–86, 2014.

[53] Schneider, C. A., Rasband, W. S., Eliceiri, K. W. NIH Image to ImageJ: 25 years of image analysis. *Nature Methods*, *9*(7): 671–675, 2012.

[54] Soumya, S., Swapna, M. S., Raj, V., Mahadevan Pillai, V. P., Sankararaman, S. Fractal analysis as a potential tool for surface morphology of thin films. *The European Physical Journal Plus*, *132*: 1–7, 2017.

[55] Horcas, I., Fernández, R., Gomez-Rodriguez, J. M., Colchero, J., Gómez-Herrero, J., Baro, A. M. WSxM: A software for scanning probe microscopy and a tool for nanotechnology. *Review of scientific instruments*, *78*(1): 013705, 2007.

[56] Frost, F., Schindler, A., Bigl, F. Roughness evolution of ion sputtered rotating InP surfaces: pattern formation and scaling laws. *Physical Review Letters*, *85*(19): 4116, 2000.

[57] Liu, L., Li, X., Nonaka, K. Light depolarization in off-specular reflection on submicro rough metal surfaces with imperfectly random roughness. *Review of Scientific Instruments*, *86*(2): 023107, 2015.